AGU PUBLICATIONS

JGR

Journal of Geophysical Research: Oceans

RESEARCH ARTICLE

10.1002/2017JC013711

Estimation of Antarctic Land-Fast Sea Ice Algal Biomass and Snow Thickness From Under-Ice Radiance Spectra in Two Contrasting Areas

P. Wongpan[1], K. M. Meiners[2,3], P. J. Langhorne[1], P. Heil[2,3], I. J. Smith[1], G. H. Leonard[4], R. A. Massom[2,3], L. A. Clementson[5], and T. G. Haskell[6]

[1]Department of Physics, University of Otago, Dunedin, New Zealand, [2]Department of the Environment and Energy, Australian Antarctic Division, Kingston, Tasmania, Australia, [3]Antarctic Climate and Ecosystems Cooperative Research Centre, University of Tasmania, Hobart, Tasmania, Australia, [4]National School of Surveying, University of Otago, Dunedin, New Zealand, [5]CSIRO Oceans and Atmosphere, Castray Esplanade, Hobart, Tasmania, Australia, [6]Callaghan Innovation, Lower Hutt, Wellington, New Zealand

Key Points:
- New algorithms to estimate Antarctic land-fast sea ice algal biomass and snow thickness from under-ice radiance spectra
- The algorithms were developed for high biomass regimes in columnar and incorporated platelet ice
- Inclusion of chlorophyll *a*-specific ice algal absorbance and pigment packaging slightly affect biomass predictability

Correspondence to:
P. Wongpan,
pat.wongpan@postgrad.otago.ac.nz

Citation:
Wongpan, P., Meiners, K. M., Langhorne, P. J., Heil, P., Smith, I. J., Leonard, G. H., et al. (2018). Estimation of Antarctic land-fast sea ice algal biomass and snow thickness from under-ice radiance spectra in two contrasting areas. *Journal of Geophysical Research: Oceans*, *123*, 1907–1923. https://doi.org/10.1002/2017JC013711

Received 14 DEC 2017
Accepted 17 FEB 2018
Accepted article online 23 FEB 2018
Published online 10 MAR 2018

Abstract Fast ice is an important component of Antarctic coastal marine ecosystems, providing a prolific habitat for ice algal communities. This work examines the relationships between normalized difference indices (NDI) calculated from under-ice radiance measurements and sea ice algal biomass and snow thickness for Antarctic fast ice. While this technique has been calibrated to assess biomass in Arctic fast ice and pack ice, as well as Antarctic pack ice, relationships are currently lacking for Antarctic fast ice characterized by bottom ice algae communities with high algal biomass. We analyze measurements along transects at two contrasting Antarctic fast ice sites in terms of platelet ice presence: near and distant from an ice shelf, i.e., in McMurdo Sound and off Davis Station, respectively. Snow and ice thickness, and ice salinity and temperature measurements support our paired in situ optical and biological measurements. Analyses show that NDI wavelength pairs near the first chlorophyll *a* (chl *a*) absorption peak (≈440 nm) explain up to 70% of the total variability in algal biomass. Eighty-eight percent of snow thickness variability is explained using an NDI with a wavelength pair of 648 and 567 nm. Accounting for pigment packaging effects by including the ratio of chl *a*-specific absorption coefficients improved the NDI-based algal biomass estimation only slightly. Our new observation-based algorithms can be used to estimate Antarctic fast ice algal biomass and snow thickness noninvasively, for example, by using moored sensors (time series) or mapping their spatial distributions using underwater vehicles.

1. Introduction

Land-fast sea ice (fast ice) is an important feature of Antarctic coastal icescapes (Fraser et al., 2012) and plays a key role in biogeochemical cycles and marine ecosystem function (Arrigo, 2017). Forming a thin barrier between the ocean and the atmosphere, fast ice affects regional sea ice production (Tamura et al., 2016), forms a temporary reservoir for nutrients (de Jong et al., 2013), and controls the amount of light available for local pelagic primary production (Perovich, 2017). Fast ice also serves as a habitat for microalgal communities, which can contribute up to 50% to the overall primary production of fast ice-covered areas (McMinn et al., 2010). Fast ice algal communities are generally concentrated in the lowermost portion of the ice, which is typically characterized by the highly porous, 0.02–0.03 m-thick skeletal layer (Weeks, 2010). The bottom communities are positioned in an optimal location to receive irradiance transmitted through the ice, colonize an environment with low variability in temperature and salinity, and have access to replenishment of nutrients from the underlying seawater. Extremely high ice algal biomass values have been reported for Antarctic fast ice containing platelet ice (Arrigo et al., 1995; Günther & Dieckmann, 1999), which forms from supercooled Ice Shelf Water (Langhorne et al., 2015, and references therein) at the base of fast ice adjacent to ice shelves (Crocker & Wadhams, 1989; Moreçki, 1965). This friable, highly porous sub-ice platelet layer provides a large surface area that serves as an important algal microhabitat. Over time, it partially solidifies to form incorporated platelet ice (e.g., Gow et al., 1982; Smith et al., 2001).

During early spring (October–November), Antarctic fast ice basal layers generally provide a habitat for well over 90% of the total integrated fast ice algal biomass (Arrigo et al., 1993; McMinn et al., 2010). Although this is a low light environment, the algal communities acclimate by modifying their photosynthetic apparatus through increasing intracellular levels of chlorophyll *a* (chl *a*) as well as accessory pigments, contributing to so-called "pigment packaging" (Arrigo et al., 1993, 2014). In self-shaded sea ice habitats where there is concentrated biomass, such as the sub-ice platelet layer (Arrigo et al., 1993), this adaptation enhances the algal light-capturing capacity by packaging more chl *a* per cell and simultaneously decreasing the absorption efficiency per unit pigment. Pigment packaging is also affected by cell size (e.g., Duysens, 1956; Morel & Bricaud, 1981).

The high spatial variability of ice algal distribution has greatly hampered accurate in situ estimation of ice algal biomass on relevant scales using classical sampling methods such as ice coring which is both time consuming and limited in areal coverage (Lange et al., 2016; Meiners et al., 2017; Mundy et al., 2007). Ice coring is also destructive and thus not well suited for time series measurements of ice algal development in a single location (Campbell et al., 2014). Here we extend methods based on the effect of ice algal photosynthetic pigments on the spectral composition of the under-ice light field through absorption of specific wavelengths in the range of photosynthetically active radiation (PAR, 400–700 nm; e.g., Arrigo & Sullivan, 1994; Fritsen et al., 2011; Hawes et al., 2012; Lange et al., 2016; Perovich et al., 1993).

A number of recent studies have explored the use of under-ice spectra to develop algorithms to estimate sea ice algal chl *a* (as a proxy for biomass) from spectral under-ice irradiance or radiance data. Mundy et al. (2007) were the first to employ normalized difference indices (NDI) of under-ice light spectra to investigate the influence of both ice algal biomass (i.e., chl *a*) and snow thickness on transmitted irradiance spectra under Arctic fast ice. Their study showed that snow has little effect on transmitted under-ice irradiances in the wavelength range of 400–570 nm and that a single NDI wavelength pair of 485:472 nm explained 89% of the ice algal variability observed in Arctic fast ice. Campbell et al. (2014) applied this NDI approach to monitor changes in basal chl *a* concentration in Arctic fast ice. Their study highlighted the need for regional calibration of NDI algorithms, i.e., regional adjustment for NDI-to-ice algal chl *a* conversions. Using an alternative numerical method, Lange et al. (2016) recently described under-ice irradiance-chl *a* relationships for Arctic pack ice by an Empirical Orthogonal Function (EOF) approach.

For Antarctica, Melbourne-Thomas et al. (2015) provided regional NDI-to-sea ice chl *a* conversion algorithms for pack ice in two contrasting regions of the Southern Ocean, while Forrest et al. (2016) provided an initial algorithm for fast ice in McMurdo Sound (Ross Sea). Taken together, these studies suggest that NDI-chl *a* relationships vary regionally and cannot be applied universally as absorption of light might be influenced by characteristics other than total biomass and may, in particular, be influenced by variable ice algal pigment packaging. Nonetheless, with sufficient information, it may eventually be possible to obtain a "global" algorithm for sea ice algal biomass. Such an algorithm has been constructed to predict ocean chl *a* concentrations using satellite-derived ocean color (O'Reilly et al., 1998).

By investigating relationships between sea ice physical properties, ice algal absorbance spectra and under-ice irradiance spectra at similar times of the year, the aim of the present study is to develop and evaluate the first NDI-ice algal chl *a* algorithms for two contrasting Antarctic fast ice areas (Figure 1). Both are characterized by very high algal standing stocks, i.e., up to an order of magnitude higher than observed in any of the previous NDI studies. One, however, was near the McMurdo Ice Shelf, Ross Sea, and was characterized by the presence of platelet ice, while the other site off Davis Station, East Antarctica, was influenced by neither an ice shelf nor platelet ice formation. Furthermore, we provide a first assessment of the effects of pigment packaging on NDI-ice algal biomass relationships. We also apply this technique to the estimation of snow thickness, which is in itself an important parameter (both physical and biological) that requires more extensive measurements (Sturm & Massom, 2017).

2. Data and Methods

2.1. Study Sites

A total of 67 paired under-ice radiance measurements and ice core samples were collected from 2 transects on Antarctic fast ice in McMurdo Sound (MS1 and MS2; $N = 24$) and 4 transects off Davis Station (DS1, DS2, DS3, and DS4; $N = 43$) in November 2014 and in November–December 2015, respectively (see Figure 1).

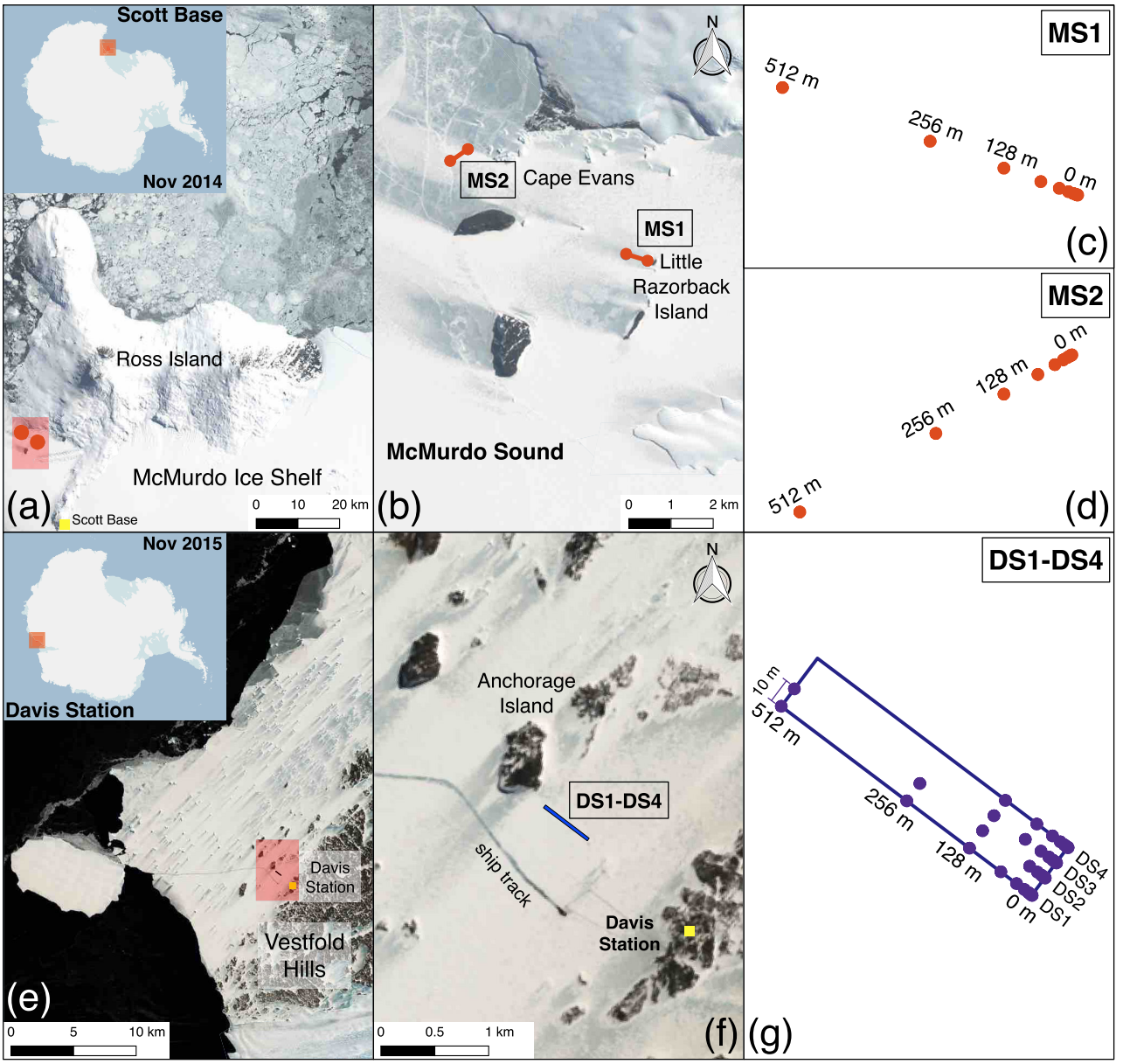

Figure 1. Maps showing six transects described in this paper MS1 (11 November 2014), MS2 (16 November 2014), DS1 (19 November 2015), DS2 (27 November 2015), DS3 (29 November 2015), and DS4 (3 December 2015) with 12, 12, 12, 11, 10, and 10 holes, respectively. (a) Scott Base in November 2014. (b) Enlarged view of the red rectangle in Figure 1a. (c, d) Details of site MS1 (at 0 m: 77.668°S; 166.524°E, and at 512 m: 77.667°S; 166.503°E) and MS2 (at 0 m: 77.644°S; 166.349°E, and at 512 m: 77.646°S; 166.331°E), respectively, in Figure 1b. (e) Davis Station in November 2015. (f) Enlarged view of the rectangle in Figure 1e. (g) Sites DS1–DS4 are 10 m apart (DS1 at 0 m: 68.569°S; 77.945°E, and at 128 m: 68.568°S; 77.943°E). Note that for each transect, 12 holes are at 0, 0.5, 1, 2, 4, 8, 16, 32, 64, 128, 256, and 512 m except for DS3 and DS4 where transects finished at 128 m. Note also that the data at 64 m DS2 were excluded from the analysis. Landsat 8 satellite acquisition dates are 10 November 2014 and 17 November 2015 for Scott Base and Davis Station, respectively. Images were pan sharpened and overlaid on Quantarctica v2.0, a free GIS package for Antarctica (http://quantarctica.npolar.no/).

Both the McMurdo Sound and Davis Station bio-optical sampling areas resembled undeformed first-year land-fast sea ice and were free of any surface disturbances.

2.2. Integrated Physical and Biological Measurements

2.2.1. In Situ Measurements

Figure 2 illustrates the integrated physical and biological measurement techniques in McMurdo Sound (MS) and at Davis Station (DS). At each sampling site, we deployed a TriOS Ramses ARC VIS radiometer (radiance

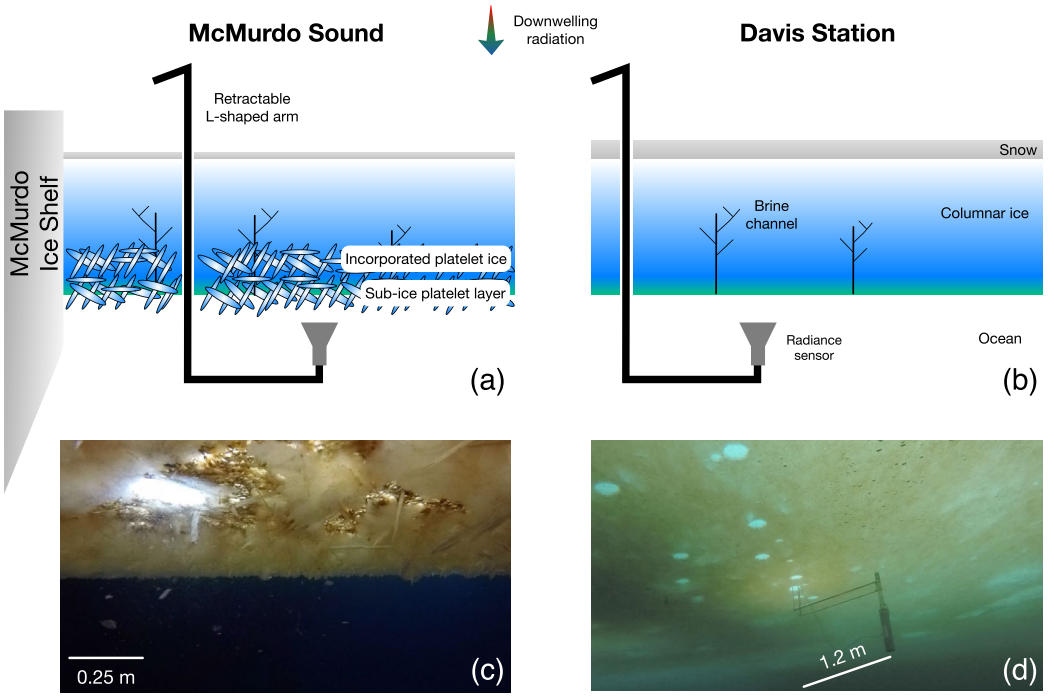

Figure 2. (a, b) Schematics of measurements in McMurdo Sound (MS1 and MS2) and Davis Station (DS1–DS4). (c, d) Upward-looking photographs of the sea ice-water interface in McMurdo Sound and near Davis Station (with deployed radiometer).

sensor, 7° field of view) 0.15 m beneath the bottom of the ice through small access holes (diameter 0.11 and 0.25 m at DS and MS, respectively) using a retractable L-shaped stainless steel arm (shown in Figure 2d). The effect of the holes in contaminating light measurements was assumed to be negligible due to the position of the radiometer 1.2 m north (i.e., directed toward the sun) of the access hole (Melbourne-Thomas et al., 2015). Under-ice high resolution radiance spectra (320–950 nm, 3.3 nm bandwidth) were recorded with a laptop computer using TriOS MSDA_XE software version 7.5.1. Results reported here represent average spectra from three or more replicate spectral measurements.

Following the radiance measurements, snow thickness was measured with a ruler (0.001 m gradation, five replicate measurements) at each site and one ice core was collected directly above the radiometer location, using a Kovacs Mark II ice corer (0.09 m internal diameter). The total length of the ice core was recorded and the 0.1 m bottom section was cut off, placed in a clean polyethylene container, and transported to the laboratory. Sampled ice core sections were then melted at 4°C in the dark, after adding 0.2 μm filtered seawater to avoid osmotic stress (Garrison & Buck, 1986). After the ice cores had melted (24–36 h after collection), the samples were gently mixed and subsamples were taken for (a) determination of ice algal pigment concentration and (b) particulate absorption.

In parallel with the biological measurements, two additional 0.09 m diameter cores were extracted at 0 and 128 m from each transect for standard sea ice temperature, salinity, and structural measurements. One core from each site was used for thick section structural analysis in a freezer laboratory. Selected thick sections were microtomed to produce thin sections and were photographed. Temperature and salinity were measured on the other cores, with the vertical temperature profiles being recorded immediately after extraction using an OMEGA Handheld Thermometer (OMEGA Engineering; Connecticut, USA). Thereafter, the core was cut into 0.1 m sections which were placed in clean plastic jars and transported to the laboratory for further analysis. Once melted at room temperature, salinities were measured with a YSI 30 conductivity meter (YSI Inc.; Ohio, USA).

2.2.2. Ice Algal Chlorophyll *a* Concentration

For pigment analysis, 0.15–1.0 L melted ice core subsamples were filtered using 25 mm diameter glass-fiber (Whatman GF/F) filters. The filters were then frozen and stored below −80°C for analysis using

high-performance liquid chromatography (HPLC). Samples were extracted over 15–18 h in acetone before analysis by HPLC using a modified C8 column and binary gradient system with an elevated column temperature (Clementson, 2013). Chl *a* was identified by retention time and absorption spectrum from a photodiode array detector, and concentrations were determined from commercial and international standards (Sigma; DHI, Denmark).

2.2.3. Particulate (Algal and Non-algal) Absorption

For absorption analyses, melted ice core subsamples (0.15–1.0 L) were filtered onto 25 mm diameter glass-fiber (Whatman GF/F) filters. The optical density (OD) spectra of the particulate material on these filters were measured over the 350–750 nm spectral range in 0.9 nm increments, using a Cintra 404 UV/VIS dual-beam spectrophotometer equipped with an integrating sphere. The pigments on the sample filter were then extracted following the method of Kishino et al. (1985) to determine the OD of the non-algal particles in a second scan. The OD due to ice algae was derived by calculating the difference between the optical density of the total particulate and non-algal fractions. The OD measurements were converted to absorption spectra using blank filter measurements, and by first adjusting the scans to zero at 750 nm and then correcting for the path length amplification using the coefficients of Mitchell (1990). A detailed description of the method is given in Clementson et al. (2001), following ocean-optics protocols for SeaWiFS validation (Müller et al., 2003).

An exponential function was fitted to all spectra of non-algal particulate material based on

$$a_{\mathrm{nap}}(\lambda) = a_{\mathrm{nap}}(350\,\mathrm{nm})\exp\left[-S(\lambda - 350\,\mathrm{nm})\right] + b, \tag{1}$$

where $a_{\mathrm{nap}}(\lambda)$ is the residual absorption coefficient over the wavelength (λ) range 350–750 nm of the particles after methanol extraction, also referred to as absorption of non-algal particles (m^{-1}) which includes absorption of nonextractable pigments and heterotrophic protists. A nonlinear least squares technique was used to fit equation (1) to the untransformed data, where *S* and *b* are empirically determined constants. The inclusion of offset *b* allows for any baseline correction. In some samples, pigment extraction was incomplete, leaving small residual peaks in the non-algal particulate spectra at the principal chlorophyll absorption bands. To avoid distorting the fitted non-algal particulate spectra, data at these wavelengths were omitted when all spectra were fitted. Total particulate spectra were smoothed using a running box-car filter with 10 nm width, and the fitted non-algal particulate spectra were subtracted to yield the ice algae spectra.

The following parameters were then determined: $a_{\mathrm{p}}(\lambda)$ = absorption coefficient of particles (m^{-1}); $a_{\mathrm{ph}}(\lambda)$ = absorption coefficient of ice algae (m^{-1}) calculated as the difference between $a_{\mathrm{p}}(\lambda)$ and $a_{\mathrm{nap}}(\lambda)$; and the chl *a*-specific absorption coefficient of ice algae $a^{*}_{\mathrm{ph}}(\lambda)$ (m^2(mg chl *a*)$^{-1}$) which is equal to the ratio of $a_{\mathrm{ph}}(\lambda)$ and (chl *a*) concentration. Note that the resulting ice algae spectra were base corrected by subtracting absorption at 750 nm to obtain $a_{\mathrm{ph}}(\lambda)$. We used nonparametric Pearson's correlation and linear regression analyses to explore the relationships between variables.

2.3. Spectral Data Analyses

2.3.1. Normalized Difference Index

All transmitted radiance spectra were interpolated to consecutive integer (1 nm) wavelengths and restricted to the range from 400 to 700 nm. To visualize correlations between integrated chl *a* and under-ice transmitted radiance (I_T) measurements, we followed the approach of Mundy et al. (2007). We first calculated NDI for all possible wavelength pairs according to the formula:

$$\mathrm{NDI}(\lambda_1, \lambda_2) = \frac{I_T(\lambda_1) - I_T(\lambda_2)}{I_T(\lambda_1) + I_T(\lambda_2)}, \tag{2}$$

where λ_1 and λ_2 are wavelengths in the PAR range 400–700 nm. We then correlated the derived NDI values with integrated chl *a* concentrations and snow thickness data, and plotted the resultant Pearson's correlation coefficient surfaces.

2.3.2. Best NDI (λ_1, λ_2) Selection

Following Mundy et al. (2007), spectral surfaces of Pearson's correlation coefficients between NDI of under-ice transmitted radiance from all possible wavelength combinations and $\log_{10}(\mathrm{chl}\,a)$ and snow thickness were constructed for groups MS, DS, and combined MS and DS. Note that in Mundy et al. (2007), NDI is a response variable and chl *a* a predictor variable. Subsequently, Campbell et al. (2014) swapped chl *a* to

response to reflect the applicability of using NDI as a predictor. Natural logarithm was applied to chl *a* ($\ln(\text{chl}\,a)$) to deal with the high variance at high chl *a* (heteroscedasticity) in Melbourne-Thomas et al. (2015) and for model comparison purposes in Lange et al. (2016). In this study, the range of our chl *a* data set covers 3 orders of magnitude so we follow previous studies but replace $\ln(\text{chl}\,a)$ with $\log_{10}(\text{chl}\,a)$.

To derive an optimal NDI wavelength pair (λ_1, λ_2) for both chl *a* and snow, we applied the following inputs. First and in addition to the Pearson's correlation surfaces for chl *a* and snow, we constructed coefficient of determination (R^2) surfaces by using $\log_{10}(\text{chl}\,a)$ or snow thickness as a response and NDI(λ_1, λ_2) as a predictor for all wavelength pairs. Second, we only considered NDI consisting of wavebands λ_1 and λ_2 that are at least 15 nm (>3 radiometer channels) apart to ensure clear separation when detected by the RAMSES radiometer. For chl *a*, wavelengths between 405 and 550 nm avoid both edge effects and the influence of snow on transmitted radiance spectra beyond 550 nm. For snow, the optimal wavelength pairs are between 405 and 655 nm to avoid proximity to the second strong absorption peak of chl *a* at ≈670 nm (e.g., Mundy et al., 2007). In addition, the null hypothesis that $\log_{10}(\text{chl}\,a)$ is constant (i.e., does not depend on NDI(λ_1, λ_2)) was tested against the alternative hypothesis that $\log_{10}(\text{chl}\,a)$ depends linearly on NDI(λ_1, λ_2). If the *p*-value is less than a critical value (set to 0.05), then the null hypothesis is rejected at the 5% significance level.

2.3.3. Pigment Packaging Index

We sought to improve the interrelationships among NDI and chl *a* by considering the effect of pigment packaging. The chl *a*-specific absorption coefficients ($a^*_{\text{ph}}(\lambda)$ from absorption peaks centered at ≈440 and ≈676 nm) were used to construct a pigment packaging index (PPI; Arrigo et al., 2014) as

$$\text{PPI} = \frac{a^*_{\text{ph}}(440\,\text{nm})}{a^*_{\text{ph}}(676\,\text{nm})}. \tag{3}$$

The interrelationship of NDI-chl *a*-PPI was explored by using the following procedure. After selecting the best pairs of NDI for chl *a*, $\log_{10}(\text{PPI})$ was added as another predictor. The null hypothesis that $\log_{10}(\text{chl}\,a)$ depends linearly on NDI(λ_1, λ_2), was tested against the alternative hypothesis that $\log_{10}(\text{chl}\,a)$ depends on NDI(λ_1, λ_2) and $\log_{10}(\text{PPI})$.

Multiple linear regression was used to compare models with different numbers of predictors, i.e., for the chl *a* model with and without PPI, the adjusted R^2 (R^2_{adj}) was used instead of R^2 as a measure of goodness of fit, where

$$R^2_{\text{adj}} = 1 - \left[\frac{(N-1)}{(N-P-1)}\right](1-R^2), \tag{4}$$

and *P* is number of predictors excluding an intercept. R^2 continues to increase with more predictors, while it adjusts for the number of predictors (e.g., Chatterjee & Hadi, 2012). Thus, if the difference between R^2 and R^2_{adj} is small, then the model(s) do not overfit the data.

3. Results

3.1. Physical Property Measurements

We first summarize the snow and ice thickness, ice salinity, and ice temperature measurements that underpin our in situ optical and biological paired measurements. Snow cover thickness was small and less variable at McMurdo Sound (mean ± 1 standard deviation [sd, hereafter]: 0.01 ± 0.02 m; range: 0–0.11 m) compared to Davis Station (mean ± sd: 0.27 ± 0.09 m; range: 0.09–0.47 m). At the former, zero snow thickness due to wind scouring occurred at locations 0.5 and 1 m on transect MS1 and at 16 m on MS2.

Figure 3 shows plots of all temperature and salinity profiles and representative basal sea ice structures from both sampling areas. The fast ice at McMurdo Sound (MS) was thicker than that at Davis Station (DS). Ice thickness at MS sampling sites ranged between 1.91 and 2.16 m (mean ± sd: 2.03 ± 0.10 m, Figures 3a and 3b) and the sea ice was predominantly columnar first-year, with an incorporated platelet ice at the bottom. A very thin (<0.02 m) sub-ice platelet layer was observed at the base of the sea ice at some MS locations but was not sampled. The transition from columnar to incorporated platelet ice occurred at 1.75 (1.90) m and 1.78 (1.51) m for the 0 (512) m cores at MS1 and MS2, respectively. For DS sites, on the other hand, columnar sea ice was present through most of the thickness (mean ± sd: 1.55 ± 0.06 m; range:

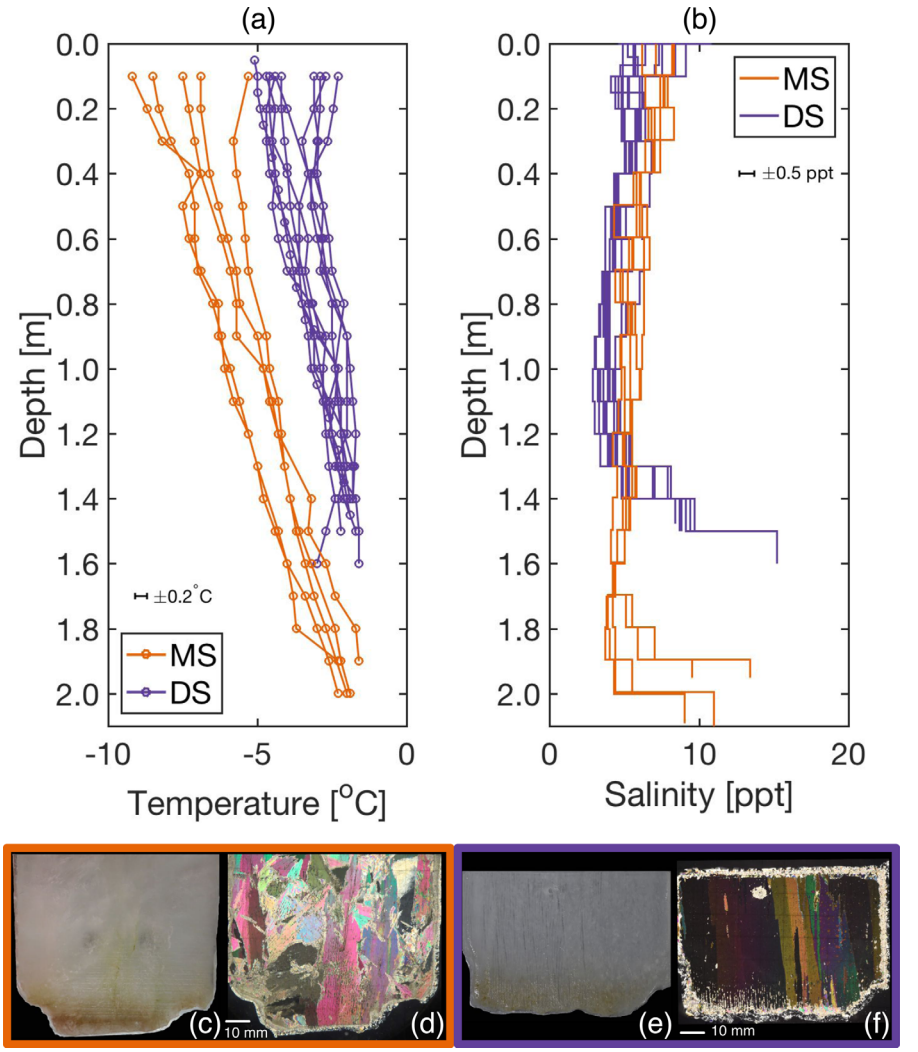

Figure 3. (a, b) Temperature (±0.2°C) and salinity (±0.5 ppt) profiles of all sampling stations. (c, d and e, f) Thick and thin sections of bottom 0.1 m ice core sections from McMurdo Sound and Davis Station, respectively. Thin sections reveal incorporated platelet ice (in Figure 3d) and columnar ice structures (in Figure 3f).

1.48–1.64 m), with a thin (∼0.1 m) layer of snow ice at the upper interface. Thus, the bottom 0.1 m sections of sea ice cores from MS were purely incorporated platelet ice (Figure 3d) while those for DS were purely columnar (Figure 3f).

Ice temperature profiles (within ±0.2°C) with depth were approximately linear during both sampling campaigns, ranging from −9.2 to −1.6°C at MS and −5.1 to −1.6°C at DS (Figure 3a). Diurnal temperature deviations from linearity were observed primarily near the sea ice surface due to the near-surface air temperature variability. Temperatures near the sea ice bottom were similar and close to the freezing temperature of seawater. Sea ice salinities (within ±0.5 ppt) ranged from 3.7 to 13.4 ppt and from 2.9 to 15.2 ppt at MS and DS, respectively (Figure 3b). Salinity profiles showed a typical C-shape with comparatively high values at the top and (particularly) the bottom of the cores.

3.2. Under-Ice Radiance Hyperspectral Measurements and Chl *a*

Mean ± sd under-ice radiance spectra normalized by the area under the curves in the 400–700 nm range for McMurdo Sound (MS; $N = 24$) and Davis Station (DS; $N = 43$) are shown in Figure 4a. Both MS and DS normalized spectra show local minima at around 440 and 675 nm at known chl *a* absorption peaks. Higher ice algal biomass reduces transmitted radiance in the blue part of the spectrum and results in a compressed peak in the green part of the spectrum (Legendre & Gosselin, 1991).

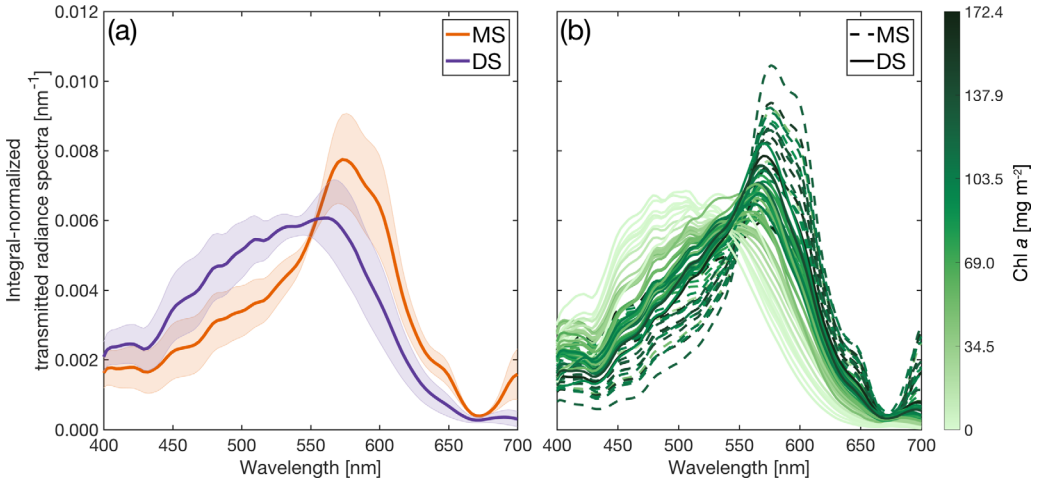

Figure 4. (a) Plot of mean ± 1 standard deviation of under-ice radiance spectra normalized by area under the curves in the 400–700 nm range with $N = 24$ and $N = 43$ for McMurdo Sound (MS) and Davis Station (DS), respectively. (b) Individual under-ice radiance spectra normalized by area under the curves were plotted in the 400–700 nm range and grouped according to ice algal chl *a* content (mg m^{-2}) in the lowermost 0.1 m of the sampled ice cores.

In McMurdo Sound, chl *a* concentrations in the lowermost 0.1 m of the cores varied between 285.4 and 2,109.5 mg m^{-3} (mean ± sd: 1,132.5 ± 414.8 mg m^{-3}). At Davis Station, concentrations were lower with a range of 2.0–1,721.0 mg m^{-3} (mean ± sd: 580.5 ± 441.8 mg m^{-3}). The corresponding ice algal chlorophyll *a* contents (integrated over the lowermost 0.1 m of the ice) ranged from 26.0 to 172.4 mg m^{-2} (mean ± sd: 105.2 ± 36.3 mg m^{-2}) and from 0.2 to 165.0 mg m^{-2} (mean ± sd: 55.1 ± 42.4 mg m^{-2}) at MS and DS, respectively (Figure 4b).

3.3. Particulate Absorption Measurements and Pigment Packaging Index

The mean and standard deviation of the absorption spectra are plotted in Figure 5 for both sites. Absorption spectra of all particulate matter (a_p) demonstrate strong absorption by chl *a* with distinct maxima at 440 and 675 nm (Figure 5a). Non-algal particulate matter spectra (a_{nap}), as shown in Figure 5b, decrease exponentially with increasing wavelength. The ice algal absorption spectra (a_{ph}) and the chl *a*-specific absorption coefficients (Figures 5c and 5d, respectively) follow the form of a_p. However, the mean of MS is smaller than that of DS due to the higher average chl *a* concentrations at MS site (Figure 5d).

The dependence of chl *a* and PPI on snow thickness is shown in Figures 6a and 6b. As defined in equation (3), PPI is constructed from the ratio of the two chl *a* absorption maxima. Values of PPI varied from 1.25 to 2.09 with a mean of 1.67±0.16 (Figure 6b). Both chl *a* and PPI are negatively correlated with snow depth, with Pearson's correlation coefficient values (ρ) of −0.69 and −0.45, respectively. The decrease in PPI indicates a flattening of the chl *a*-specific absorption spectrum, i.e., increased pigment packaging.

3.4. NDI Algorithm

Pearson's correlation coefficient surfaces (Figure 7) as well as R^2 surfaces (Figure 8) were constructed for both chl *a* and snow thickness. The strong negative relationship between biomass and snow thickness (Figure 6a) causes the filled contours of chl *a* in Figures 7a, 7c, and 7e to be approximately the inverse of snow thickness in Figures 7b, 7d, and 7f. The R^2 surfaces of Figure 8 are used as the main criteria for selecting the optimal wavelength pairs for the algorithm. Values of R^2, R^2_{adj}, and *p*-value for MS, DS, and combined MS and DS are summarized in Table 1. In particular, optimal values of $\mathrm{NDI}(\lambda_1, \lambda_2)$ of combined MS and DS for chl *a* and snow thickness are plotted in Figure 8. The best wavelength pairs are separated by 15 and 81 nm for chl *a* and snow thickness, respectively. The root-mean-squared errors of data about the best fit model are 0.4 for $\log_{10}(\mathrm{chl}\,a)$ and 0.05 m for snow thickness.

3.5. NDI-PPI-Chl *a* Interrelationships

To investigate the influence of the algal pigment packaging effect on NDI-based algal biomass estimates, R^2, R^2_{adj}, and *p*-values of a model of MS, DS, and combined MS and DS were compared with a model that included PPI as a second predictor. The results are summarized in Table 2. The relations for combined MS

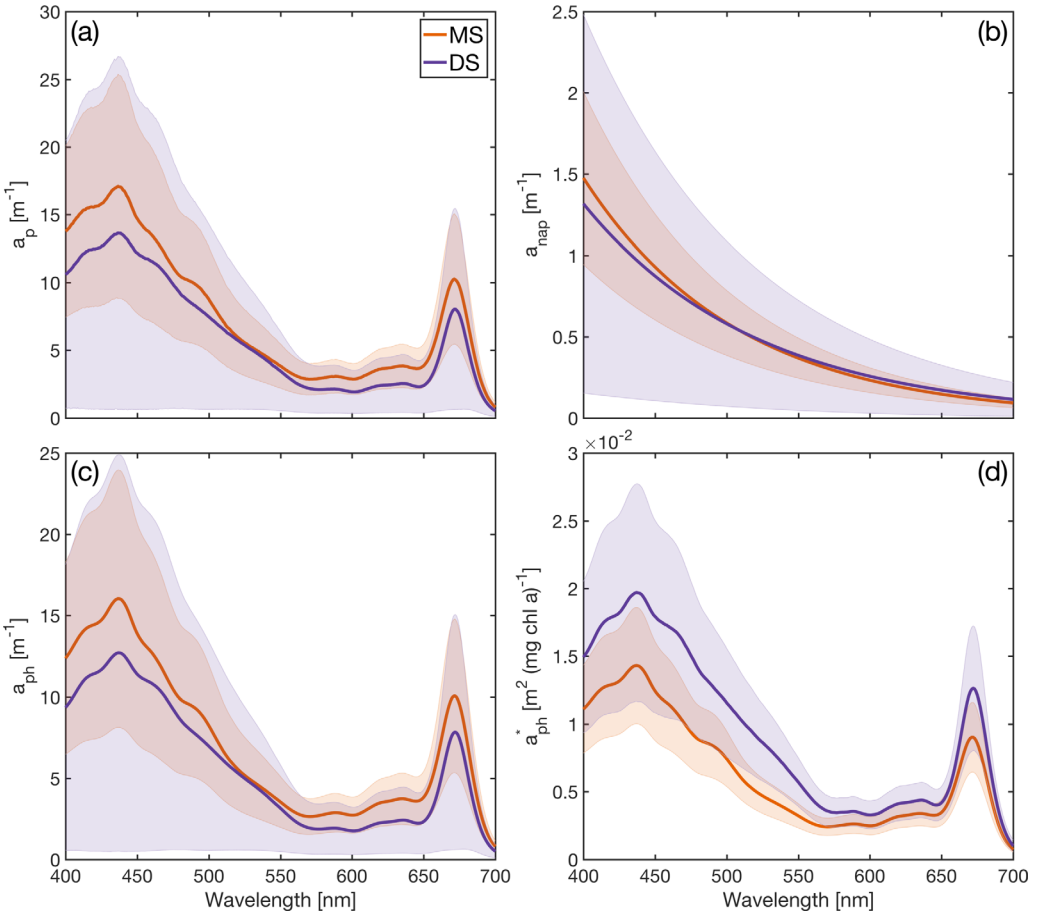

Figure 5. Plots of (a) a_p (the spectral absorption of all particulate matter), with standard deviation shown by shading; (b) a_{nap} (the spectral absorption of non-algal particulate matter); (c) a_{ph} (the spectral absorption of phytoplankton; that is ($a_p - a_{nap}$); and (d) chl *a* normalized a^*_{ph}, i.e., a_{ph}/(chl *a*(mg m^{-3})).

and DS data are shown in Figure 9. The inclusion of the second predictor $\log_{10}(\mathrm{PPI})$ increases R^2_{adj} from 0.69 to 0.74. Specifically, the significance of the $\log_{10}(\mathrm{PPI})$ term for combined MS and DS chl *a* was tested with the null hypothesis that the description of chl *a* without PPI is adequate. The *p*-value is 0.0005 ($<$0.05), rejecting the null hypothesis.

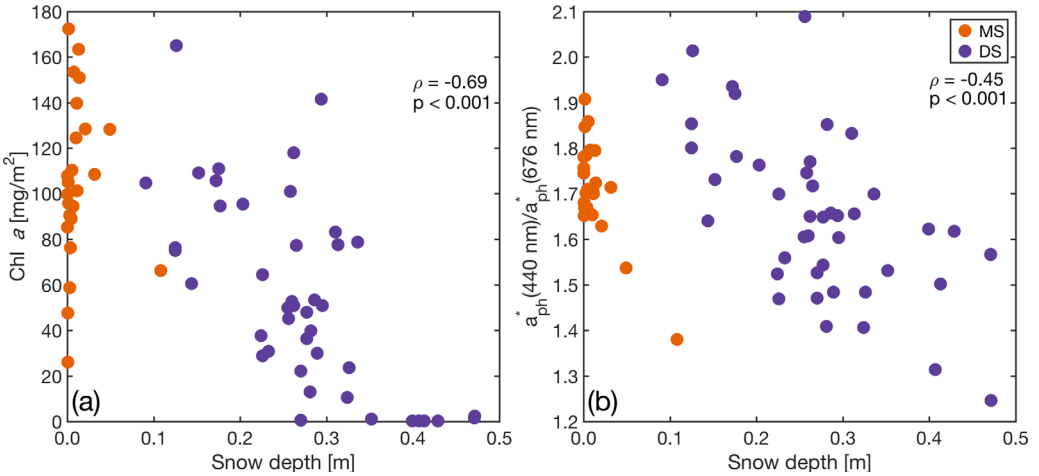

Figure 6. (a) Plot of snow depth against chl *a*. (b) Plot of snow depth against pigment packaging index (PPI) defined as $a^*_{ph}(440\ \mathrm{nm})/a^*_{ph}(676\ \mathrm{nm})$.

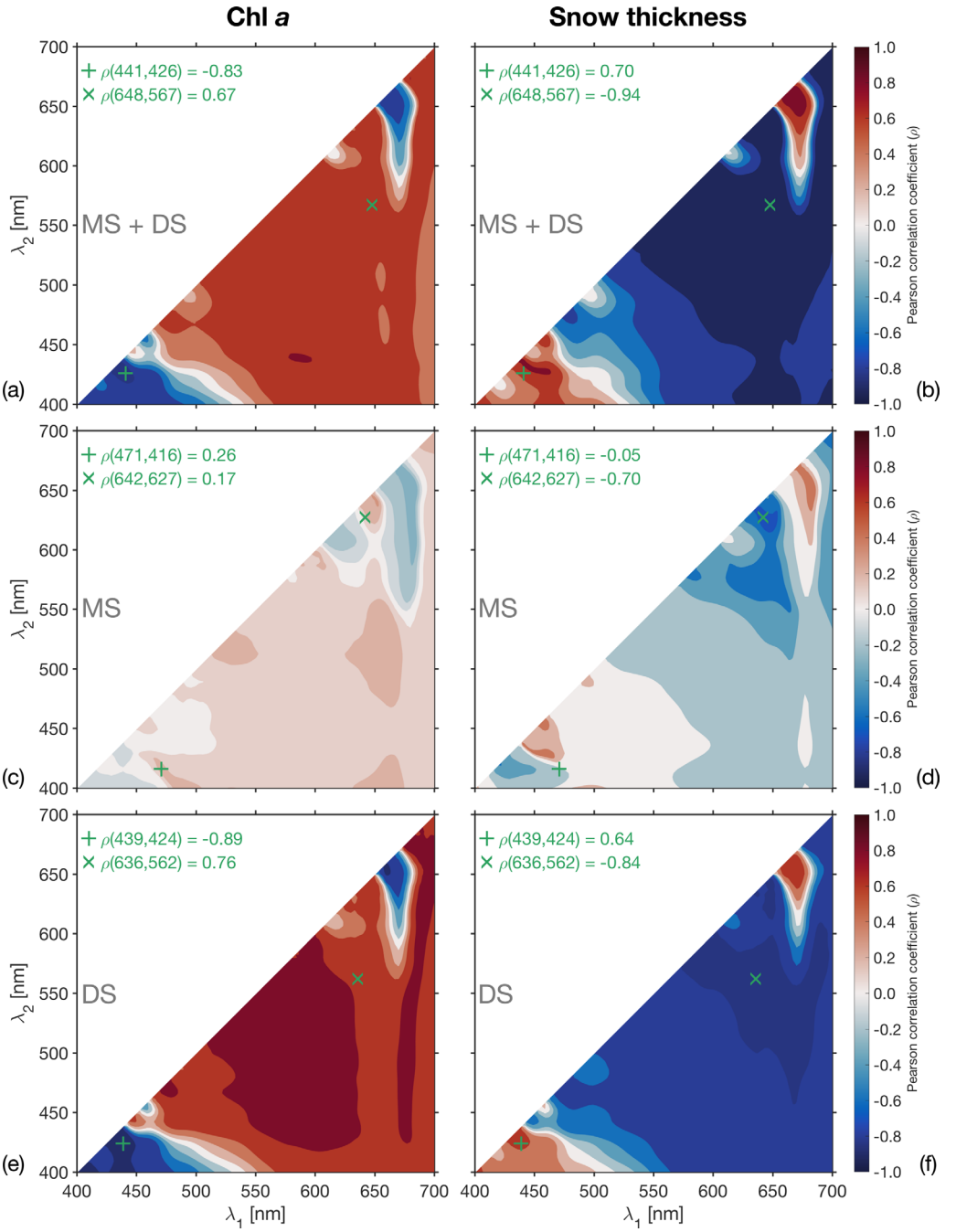

Figure 7. Correlation surface plots for normalized difference indices (for details see text) and chl *a* and snow data. Pearson's correlation coefficient for (a, b) combined MS and DS; (c, d) MS; and (e, f) DS for chl *a* and snow thickness. Note that values of Pearson's correlation coefficients for best wavelength pairs of combined MS and DS for chl *a* (plus) and snow thickness (cross) are also shown.

4. Discussion

Our study provides empirical algorithms to estimate sea ice algal chl *a* content and snow thickness from under-ice radiance measurements at two physically different Antarctic fast ice locations that were both characterized by high ice algal biomass standing stocks.

The physical contrast between the MS and DS sites is mainly due to the difference in snow thickness and the presence of an incorporated platelet ice layer at MS. The sea ice at MS was thicker than at DS, partly

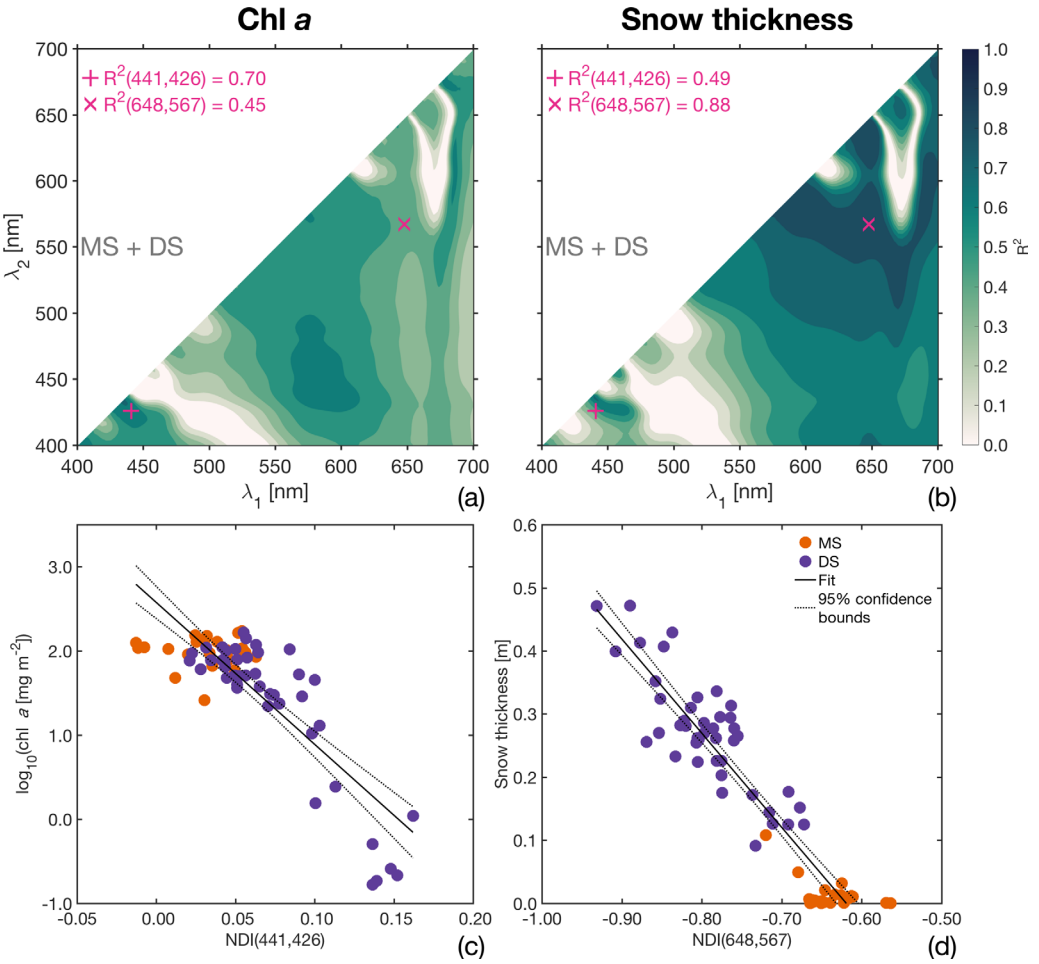

Figure 8. (a, b) R^2 correlation surfaces of combined MS and DS data sets for both chl *a* and snow thickness, respectively. Note that values of R^2 for best wavelength pairs for chl *a* (plus) and snow thickness (cross) are also shown. (c, d) Relations for best NDI(λ_1, λ_2) against chl *a* and snow thickness, respectively. See Table 1 for the equations.

because the growth rate of incorporated platelet ice is greater than that of purely columnar ice (Smith et al., 2015). Salinity measurements from both sites agreed with observations reporting C-shape profiles as typical for Antarctic first-year fast ice (e.g., Eicken, 1992; Weeks, 2010). Salinities at MS corresponded with those reported by Gough et al. (2012), demonstrating only marginal differences between columnar and incorporated platelet ice.

Table 1
NDI[a] Summary

Site	*N*	Empirical relationship	R^2	R^2_{adj} [b]	*p*-Value[c]
MS	24	$\log_{10}(\text{chl } a(\text{mg m}^{-2})) = 1.27 + 3.76 \times \text{NDI}(471,416)$	0.07	0.03	0.2
		$\text{Snow (m)} = -0.20 - 1.19 \times \text{NDI}(642,627)$	0.49	0.47	<0.001
DS	43	$\log_{10}(\text{chl } a(\text{mg m}^{-2})) = 2.07 - 18.16 \times \text{NDI}(439,424)$	0.79	0.79	<0.0001
		$\text{Snow (m)} = -0.48 - 1.06 \times \text{NDI}(636,562)$	0.70	0.69	<0.0001
Both	67	$\log_{10}(\text{chl } a(\text{mg m}^{-2})) = 2.58 - 16.85 \times \text{NDI}(441,426)$	0.70	0.69	<0.0001
		$\text{Snow (m)} = -0.92 - 1.49 \times \text{NDI}(648,567)$	0.88	0.88	<0.0001

[a]NDI stands for the normalized different index. [b]R^2_{adj} is given by equation (4). [c]The null hypothesis of this *p*-value is that $\log_{10}(\text{chl } a(\text{mg m}^{-2}))$ = constant is adequate against the empirical relationship.

Table 2
NDI-PPI[a] *Summary*

Site	*N*	Empirical relationship	R^2	R^2_{adj} [b]	*p*-Value[c]
MS	24	$\log_{10}(\text{chl } a(\text{mg m}^{-2})) = 0.62 + 4.40 \times \text{NDI}(471,416) + 2.24 \times \log_{10}(\text{PPI})$	0.19	0.11	0.1
DS	43	$\log_{10}(\text{chl } a(\text{mg m}^{-2})) = 1.36 - 16.46 \times \text{NDI}(439,424) + 2.97 \times \log_{10}(\text{PPI})$	0.81	0.80	<0.0001
Both	67	$\log_{10}(\text{chl } a(\text{mg m}^{-2})) = 1.44 - 14.70 \times \text{NDI}(441,426) + 4.56 \times \log_{10}(\text{PPI})$	0.75	0.74	<0.0001

[a]NDI and PPI stand for the normalized different index, and the pigment packaging index, respectively. [b]R^2_{adj} is given by equation (4). [c]The null hypothesis of this *p*-value is that $\log_{10}(\text{chl } a(\text{mg m}^{-2}))$ = constant is adequate against the empirical relationship.

Our sea ice structural analyses suggest that the basal ice algae inhabited different ice types: incorporated platelet ice at MS and columnar ice at DS. Considering both columnar (DS) and incorporated platelet ice (MS) as congelation ice with basal skeletal layers, sea ice algae from both sites can be classified as bottom communities. The mean integrated chl *a* concentrations at MS were higher than that at DS. Ice algal biomass standing stocks are in agreement with previous studies conducted during the spring ice algal bloom period at these sites (Archer et al., 1996; Arrigo, 2017; Arrigo et al., 1995). The friable sub-ice platelet layer that preceded the incorporated platelet ice at the base of the sea ice cover in McMurdo Sound provided a porous habitat for high chl *a* accumulation (Arrigo et al., 1995; Günther & Dieckmann, 1999).

Normalized under-ice radiance spectra show local minima at around 440 and 676 nm at all stations, consistent with the in situ absorbance maxima of ice algae (e.g., Beeler SooHoo et al., 1987; Fritsen et al., 2011). Our observations confirm previous reports on the influence of ice algal biomass on under-ice spectra from both the Arctic and Antarctic (Beeler SooHoo et al., 1987; Ehn et al., 2008; Mundy et al., 2007; Perovich et al., 1993). The chl *a*-specific absorption coefficients $a^*_{ph}(\lambda)$ resemble the shape of the $a_p(\lambda)$ spectra with maximum absorption in the blue-green region of the spectrum between 430 and 530 nm, with a second narrower peak at around 676 nm (Figure 5d). An exponential decrease of $a_{nap}(\lambda)$, the non-algal particle absorption coefficient, with increasing wavelength is typical for marine detrital material (Kishino et al., 1985, Figure 5b). Variations in $a^*_{ph}(\lambda)$ have been attributed to the algal community taxonomic composition, with coupled changes in intracellular pigment concentrations and composition as well as cell size being interpreted as the pigment packaging effect (Arrigo et al., 1993; Bricaud et al., 2004). Spectra of $a^*_{ph}(\lambda)$ observed in the present study correspond to the absorption of diatoms containing chl *a* and accessory photosynthetic carotenoid pigments, particularly fucoxanthin which has maximum absorption around 450–550 nm (e.g., Arrigo et al., 1991). Diatoms generally dominate Antarctic fast ice bottom ice algal communities (Arrigo, 2014, 2017).

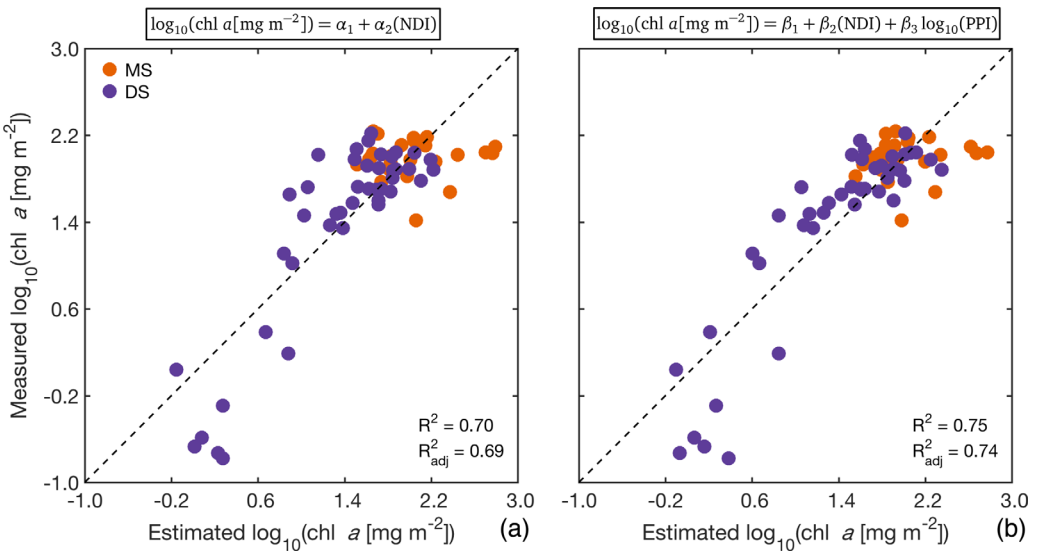

Figure 9. Comparison of empirical relationships between chl *a* and NDI (a) without PPI and (b) with PPI.

Table 3
NDI[a] Comparison

Study (location)	Sea ice type	Empirical relationship	R^2	Sampling season	Mean; max chl *a* (mg m^{-2})	Mean snow depth (m)
Present study (McMurdo Sound, Antarctica)	Fast ice (first-year)	$\log_{10}(\text{chl}\,a)=1.27+3.76\times\text{NDI}(471,416)$	0.07	Austral spring	105.2; 172.4	0.01
Present study (Davis Station, Antarctica)	Fast ice (first-year)	$\log_{10}(\text{chl}\,a)=2.07-18.16\times\text{NDI}(439,424)$	0.79	Austral spring	55.1; 165.0	0.27
Present study (both)	Fast ice (first-year)	$\log_{10}(\text{chl}\,a)=2.58-16.85\times\text{NDI}(441,426)$	0.70	Austral spring	73.0; 172.4	0.18
Lange et al. (2016)-Irradiance (Arctic)	Pack ice (multiyear and first-year)	$\ln(\text{chl}_{\text{adj}}a)=2.2+10.8\times\text{NDI}(683,669)$[b]	0.73	Arctic late summer	3.34; 11.83	<0.1
Lange et al. (2016)-Transmittance (Arctic)	Pack ice (multiyear and first-year)	$\ln(\text{chl}_{\text{adj}}a)=1.2-11.1\times\text{NDI}(684,678)$[b]	0.79	Arctic late summer	3.34; 11.83	<0.1
Melbourne-Thomas et al. (2015) (East Antarctica, Antarctica)	Pack ice (first-year)	$\ln(\text{chl}\,a)=-4.27-351\times\text{NDI}(422,418)$	0.64	Austral spring	0.84; 3.25	0.15
Melbourne-Thomas et al. (2015, 2016) (Weddell Sea, Antarctica)	Pack ice (first-year)	$\ln(\text{chl}\,a)=0.39+31.7\times\text{NDI}(479,468)$	0.79	Austral spring	6.69; 19.79	0.15
Campbell et al. (2014) (Allen Bay, Arctic)	Fast ice (first-year)	$\text{chl}\,a=15.2-497\times\text{NDI}(490,478)$	0.81	Across Arctic spring	16.8; 22.1	0.16
Mundy et al. (2007) (Resolute Bay, Arctic)	Fast ice (first-year)	$\text{chl}\,a=-8.3+1000\times\text{NDI}(485,472)$	0.89[c]	Arctic spring	30.6; 109	0.16

[a]NDI stands for the normalized different index. [b]$\text{chl}_{\text{adj}}\,a$ is an adjusted chl *a*: $\text{chl}_{\text{adj}}\,a=\text{chl}\,a+0.98$ mg m^{-2} (Lange et al., 2016). [c]R^2 was calculated from $\text{NDI}(485,472)=0.001\times\text{chl}\,a+0.0083$ using NDI as the predictor (Mundy et al., 2007).

Our empirical relationships from MS and DS and the combined data set are compared with results from previous NDI studies in Table 3. The present study fills an NDI algorithm gap for Antarctic land-fast sea ice and also provides new algorithms that are calibrated for high chl *a* regimes in columnar and platelet ice (≈73 mg m^{-2}, range: 0.2–172.4 mg m^{-2}) and snow depths ranging between 0 and 0.5 m (≈0.2 m). Specifically, our results are applicable for Antarctic fast ice which comprises mainly ice algal bottom communities. The NDI algorithms developed in Melbourne-Thomas et al. (2015, 2016) and Lange et al. (2016) have already shown the applicability of the NDI technique for pack ice environments which can comprise not only the bottom communities but also ice algal interior and surface communities (e.g., Meiners et al., 2012). However, in general chl *a* concentrations in these studies were low compared to the current study. Further work is required to test the applicability of the NDI technique to ice types with complex vertical and mixed distributions of ice algae as regularly observed in pack ice environments (see e.g., van Leeuwe et al., 2018, for a recent review).

If the area of interest is a mix of ice types then other methods (such as aerial/satellite remote sensing) could be used to determine the type of ice studied, and hence the appropriate algorithm for sea ice biomass. In ocean color remote sensing global algorithms have been applied, but increasingly regional algorithms are being developed which generally provide better estimates/products (e.g., O'Reilly et al., 1998). Here we are dealing with a similar challenge.

Considering all algorithms in Table 3 suggests that if the snow is thick enough (>0.1 m), the model selection method favors an NDI wavelength pair (for chl *a* estimation) that is closest to the first chl *a* absorption peak (≈440 nm). When the snow is thin, then model selection picks the highest correlation between NDI and chl *a* in the region of the second peak (≈670 nm). Both NDI algorithms of Lange et al. (2016) are in this category, with snow thickness less than 0.1 m. This can be interpreted as the influence of snow on NDI-based chl *a* estimates at these higher wavelengths, as previously discussed by Mundy et al. (2007). To avoid interference of the second chl *a* absorption peak on the snow algorithm, we limited the search for the best NDI-snow algorithm to be in the range 405–655 nm (Table 1). From inspection, the best NDI for snow is not close to the first chl *a* absorption peak, so we did not constrain the lower bound to avoid its interference with the algorithm.

As stated by Mundy et al. (2007) and illustrated in our R^2 surfaces, the NDI wavelength range between 400 and 550 nm is not well correlated with snow depth. Our NDI(441,426) correlates well with chl *a* ($\rho=-0.83$) and less with snow ($\rho=0.70$; Figures 7a and 7b). Compared to DS, the optimal wavelength pair of MS was positioned at higher wavelengths than the first chl *a* absorption peak (>440 nm). This is consistent with the findings of Beeler SooHoo et al. (1987), who reported enhanced absorption of platelet ice algae in the 450–550 nm wavelength range.

Our mean PPI (1.67 ± 0.16) agrees with PPI values (2.02 ± 0.46) reported for bottom ice algal communities in Amundsen Sea pack ice (Arrigo et al., 2014). The PPI model's difference in R^2 and R^2_{adj} is small and demonstrates that the model does not overfit the data by adding $\log_{10}(\mathrm{PPI})$ as the second predictor after NDI. The p-value for the $\log_{10}(\mathrm{PPI})$ term is 0.0005 (<0.05), implying that this term is significant at the 5% significance level for combined MS and DS. For the combined MS and DS data set, inclusion of the predictor $\log_{10}(\mathrm{PPI})$ improves the R^2_{adj} for chl *a* by up to 0.05 (see Tables 1 and 2). Given this small improvement and the considerable effort needed for ice algae absorption measurements, we suggest that the inclusion of PPI can possibly be neglected for fast ice. However, the inclusion of PPI may become important when constructing integrated multiparameter algorithms involving different sea ice types (e.g., pack ice and fast ice) that have higher variability of PPI due to different sea ice algal habitats (e.g., Arrigo et al., 2014). Recently, Kauko et al. (2017) also suggested that in Arctic leads, both light and algal species composition influence pigment packaging.

Another way to improve the performance of optical algorithms to estimate ice algal biomass was recently proposed by Lange et al. (2016) who suggested the application of the EOF approach over NDI and proposed using transmittance data for algorithm development based on Nicolaus and Katlein (2013). Our R^2 values from NDI algorithms are similar to those reported in the study of Lange et al. (2016) (73% for NDI-irradiance and 70% for NDI-transmittance). However, the wavelengths selected for the NDI algorithms of Lange et al. (2016) are close to the second chl *a* absorption peak at 670 nm which correlates with snow thickness (e.g., Mundy et al., 2007). Note that the NDI algorithms of Lange et al. (2016) were calibrated with both thin snow thickness data (<0.1 m) and low biomass. This might limit their applicability to Arctic sea ice with a thin snow cover, e.g., late summer conditions when most of their data were collected. In Antarctic pack ice, the NDI algorithms in Melbourne-Thomas et al. (2015) were optimized for low chl *a* concentrations and thicker snow. Compared with other algorithms, including the EOF, they show relatively high R^2 values for the NDI method. Lange et al. (2016) also suggested normalizing spectra to their corresponding downwelling irradiance when dealing with data sets taken over larger areas and during different seasons. This is particularly true for Arctic sea ice that shows strong seasonal changes in surface conditions, i.e., changing from snow cover to white ice and melt ponds before breaking up.

A relatively poor NDI-to-chl *a* relationship was observed for the MS study site. We attribute this to (i) the low overall variability in algal biomass in this particular data set and (ii) potential biases in sampling the fragile unconsolidated sub-ice platelet layer at the bottom of MS ice cores. Further work is required to advance quantitatively robust sampling techniques for platelet ice and to develop optical methods to understand the phenology of platelet ice algal communities as well as their spatial variability (Forrest et al., 2016). Many of the MS sites also showed zero to very low snow depths but variable chl *a* content, suggesting that factors other than snow control ice algal biomass accumulation in this area. The variability most likely relates to processes within the sub-ice platelet layer habitat (Figure 2c) in which crystal structure and surface area, as well as nutrient availability within the porous ice matrix, are important for algal colonization (e.g., Arrigo, 2017).

Our results show that chl *a* was negatively correlated with snow depth. Strong inverse relationships between snow cover thickness and ice algal standing stock have been reported elsewhere for Antarctic sea ice habitats (Ackley & Sullivan, 1994; Grossi & Sullivan, 1985). For Arctic fast ice, a seasonally changing influence of snow on ice algal standing stocks has been described (Leu et al., 2015; Mundy et al., 2005). There, snow limits light availability early in the ice-growth season, but the relationship reverses later in the season, i.e., in boreal spring, because the snow cover prevents basal ice ablation, thereby stabilizing the ice algal habitat (Campbell et al., 2015). Thereafter, formation of melt ponds during summer allows higher light transmittance into Arctic sea ice (e.g., Nicolaus et al., 2012). Surface melt pond formation is rare on Antarctic sea ice (Andreas & Ackley, 1982; Sturm & Massom, 2017). A comparative description of ice algal phenology is lacking for Antarctic fast ice and future research is needed to investigate a potentially seasonally changing snow-chl *a* relationship in Antarctic sea ice (Meiners et al., 2017).

5. Conclusion

In conclusion, our study provides a first bio-optical investigation of first-year fast ice from two contrasting areas of the Antarctic coast. The contrasts between the two sites were mainly due to a higher variation in snow thickness at Davis Station sites, and the presence of the incorporated platelet ice at McMurdo Sound

sites due to the influence of the McMurdo Ice Shelf. The NDI algorithm developed explains 70% of chl *a* for combined MS and DS data with wavelength pairs that are close to the first absorption peak of chl *a* at around 440 nm. This result is consistent with observations in earlier studies and extends the NDI algorithm toward a high chl *a* regime. Furthermore, NDI-based predictability of algal biomass can be improved by up to 5% when the ratio of chl *a*-specific absorption of both peaks is included in the model.

Another important finding was that the NDI developed from the wavelength combination above 550 nm and below the second chl *a* absorption peak describes 88% of the variation in the combined MS and DS snow thickness data. Our empirical relationship for the MS site was limited, however, and future work is required to develop robust relationships for sea ice with a significant platelet ice component. The interrelationships of chl *a*, snow and NDI provide an important step toward developing a calibrated toolbox to obtain chl *a* and potentially snow depth at local to regional scales using remotely operated or autonomous underwater vehicles. Deployment of hyperspectral under-ice radiometers provides a noninvasive tool for ice algal biomass determination. Such radiometers should be routinely incorporated into physical sea ice mass balance stations collecting data throughout the sea ice season to further our understanding of coupled sea ice physical-biological processes and ice algal phenologies in polar ecosystems.

Acknowledgments

We gratefully acknowledge logistic support by the Australian Antarctic Division and Antarctica New Zealand, and the crews of Davis Station and Scott Base. P.W. was supported by University of Otago Postgraduate Scholarship. This study was supported by the Australian Government through (i) Australian Antarctic Science project #4298 and (ii) the Cooperative Research Centre Programme through the Antarctic Climate and Ecosystems Cooperative Research Centre (ACE CRC); and (iii) University of Otago research grants 110282 and 112061, (iv) a subcontract *Antarctic and High Latitude Climate* to NIWA, and (iv) the New Zealand Deep South National Science Challenge. P.W. and P.J.L. are very grateful to the Institute for Marine and Antarctic Studies where data were analyzed. Work on this paper was undertaken while P.J.L. enjoyed the support and hospitality of the Alfred Wegener Institute, Germany, and of the Isaac Newton Institute for Mathematical Sciences, Cambridge, during the Mathematics of Sea Ice Phenomena (supported by EPSRC grant EP/K032208/1). K.M.'s contribution was supported through a fellowship at the Hanse-Wissenschaftskolleg (Delmenhorst, Germany). We are very grateful for the field support of Mark Milnes (AAD).

Data availability. All data used in this study are available through the Australian Antarctic Data Centre (AADC) at https://data.aad.gov.au.

References

Ackley, S., & Sullivan, C. (1994). Physical controls on the development and characteristics of Antarctic sea ice biological communities—A review and synthesis. *Deep Sea Research Part I: Oceanographic Research Papers*, *41*(10), 1583–1604. https://doi.org/10.1016/0967-0637(94)90062-0

Andreas, E. L., & Ackley, S. F. (1982). On the differences in ablation seasons of Arctic and Antarctic sea ice. *Journal of the Atmospheric Sciences*, *39*(2), 440–447. https://doi.org/10.1175/1520-0469(1982)039<0440:OTDIAS>2.0.CO;2

Archer, S., Leakey, R., Burkill, P., Sleigh, M., & Appleby, C. (1996). Microbial ecology of sea ice at a coastal Antarctic site: Community composition, biomass and temporal change. *Marine Ecology Progress Series*, *135*, 179–195. https://doi.org/10.3354/meps135179

Arrigo, K. R. (2014). Sea ice ecosystems. *Annual Review of Marine Science*, *6*(1), 439–467. https://doi.org/10.1146/annurev-marine-010213-135103

Arrigo, K. R. (2017). Sea ice as a habitat for primary producers. In D. N. Thomas (Ed.), *Sea ice* (pp. 352–369). Hoboken, NJ: John Wiley. https://doi.org/10.1002/9781118778371.ch14

Arrigo, K. R., Brown, Z. W., & Mills, M. M. (2014). Sea ice algal biomass and physiology in the Amundsen Sea, Antarctica. *Elementa: Science of the Anthropocene*, *2*, 000028. https://doi.org/10.12952/journal.elementa.000028

Arrigo, K. R., Dieckmann, G., Gosselin, M., Robinson, D. H., Fritsen, C. H., & Sullivan, C. W. (1995). High resolution study of the platelet ice ecosystem in McMurdo Sound, Antarctica: Biomass, nutrient, and production profiles within a dense microalgal bloom. *Marine Ecology Progress Series*, *127*, 255–268. https://doi.org/10.3354/meps127255

Arrigo, K. R., Robinson, D. H., & Sullivan, C. W. (1993). High resolution study of the platelet ice ecosystem in McMurdo Sound, Antarctica: Photosynthetic and biooptical characteristics of a dense microalgal bloom. *Marine Ecology Progress Series*, *98*, 173–185. https://doi.org/10.3354/meps098173

Arrigo, K. R., & Sullivan, C. W. (1994). A high resolution bio-optical model of microalgal growth: Tests using sea-ice algal community time-series data. *Limnology and Oceanography*, *39*(3), 609–631. https://doi.org/10.4319/lo.1994.39.3.0609

Arrigo, K. R., Sullivan, C. W., & Kremer, J. N. (1991). A bio-optical model of Antarctic sea ice. *Journal of Geophysical Research*, *96*(C6), 10581. https://doi.org/10.1029/91JC00455

Beeler SooHoo, J., Palmisano, A. C., Kottmeier, S. T., Lizotte, M. P., SooHoo, S. L., & Sullivan, C. W. (1987). Spectral light absorption and quantum yield of photosynthesis in sea ice microalgae and a bloom of Phaeocystis pouchetii from Mcmurdo Sound, Antarctica. *Marine Ecology Progress Series*, *39*, 175–189. https://doi.org/10.3354/meps039175

Bricaud, A., Claustre, H., Ras, J., & Oubelkheir, K. (2004). Natural variability of phytoplanktonic absorption in oceanic waters: Influence of the size structure of algal populations. *Journal of Geophysical Research*, *109*, C11010. https://doi.org/10.1029/2004JC002419

Campbell, K., Mundy, C., Barber, D., & Gosselin, M. (2015). Characterizing the sea ice algae chlorophyll *a*—Snow depth relationship over Arctic spring melt using transmitted irradiance. *Journal of Marine Systems*, *147*, 76–84. https://doi.org/10.1016/j.jmarsys.2014.01.008

Campbell, K., Mundy, C. J., Barber, D. G., & Gosselin, M. (2014). Remote estimates of ice algae biomass and their response to environmental conditions during spring melt. *Arctic*, *67*(3), 375. https://doi.org/10.14430/arctic4409

Chatterjee, S., & Hadi, A. S. (2012). *Regression analysis by example*. Hoboken, NJ: John Wiley.

Clementson, L. A. (2013). The CSIRO method. In S. B. Hooker et al. (Eds.), *The fifth SeaWiFS HPLC Analysis Round-Robin Experiment (SeaHARRE-5)* (NASA Tech. Memo. 2012–217503). Greenbelt, MD: NASA Goddard Space Flight Center.

Clementson, L. A., Parslow, J. S., Turnbull, A. R., McKenzie, D. C., & Rathbone, C. E. (2001). Optical properties of waters in the Australasian sector of the Southern Ocean. *Journal of Geophysical Research*, *106*(C12), 31611–31625. https://doi.org/10.1029/2000JC000359

Crocker, G., & Wadhams, P. (1989). Modelling Antarctic fast-ice growth. *Journal of Glaciology*, *35*(119), 3–8. https://doi.org/10.3189/002214389793701590

de Jong, J., Schoemann, V., Maricq, N., Mattielli, N., Langhorne, P., Haskell, T., et al. (2013). Iron in land-fast sea ice of McMurdo Sound derived from sediment resuspension and wind-blown dust attributes to primary productivity in the Ross Sea, Antarctica. *Marine Chemistry*, *157*, 24–40. https://doi.org/10.1016/j.marchem.2013.07.001

Duysens, L. (1956). The flattening of the absorption spectrum of suspensions, as compared to that of solutions. *Biochimica et Biophysica Acta*, *19*, 1–12. https://doi.org/10.1016/0006-3002(56)90380-8

Ehn, J. K., Mundy, C. J., & Barber, D. G. (2008). Bio-optical and structural properties inferred from irradiance measurements within the bottommost layers in an Arctic landfast sea ice cover. *Journal of Geophysical Research*, *113*, C03S03. https://doi.org/10.1029/2007JC004194

Eicken, H. (1992). Salinity profiles of Antarctic sea ice: Field data and model results. *Journal of Geophysical Research*, *97*(C10), 15545. https://doi.org/10.1029/92JC01588

Forrest, A. L., Lund-Hansen, L. C., Sorrell, B. K., Bowden-Floyd, I., Lucieer, V., Cossu, R., et al. (2016). Brief communication: Capturing scales of spatial heterogeneity of Antarctic sea ice algae communities. *The Cryosphere Discussions*, 1–13. https://doi.org/10.5194/tc-2016-186

Fraser, A. D., Massom, R. A., Michael, K. J., Galton-Fenzi, B. K., & Lieser, J. L. (2012). East Antarctic landfast sea ice distribution and variability, 2000–08. *Journal of Climate*, *25*(4), 1137–1156. https://doi.org/10.1175/JCLI-D-10-05032.1

Fritsen, C. H., Wirthlin, E. D., Momberg, D. K., Lewis, M. J., & Ackley, S. F. (2011). Bio-optical properties of Antarctic pack ice in the early austral spring. *Deep Sea Research Part II: Topical Studies in Oceanography*, *58*(9–10), 1052–1061. https://doi.org/10.1016/j.dsr2.2010.10.028

Garrison, D. L., & Buck, K. R. (1986). Organism losses during ice melting: A serious bias in sea ice community studies. *Polar Biology*, *6*(4), 237–239. https://doi.org/10.1007/BF00443401

Gough, A. J., Mahoney, A. R., Langhorne, P. J., Williams, M. J. M., & Haskell, T. G. (2012). Sea ice salinity and structure: A winter time series of salinity and its distribution. *Journal of Geophysical Research*, *117*, C03008. https://doi.org/10.1029/2011JC007527

Gow, A., Ackley, S., Weeks, W., & Govoni, J. (1982). Physical and structural characteristics of Antarctic sea ice. *Annals of Glaciology*, *3*, 113–117. https://doi.org/10.1017/S0260305500002627

Grossi, S. M., & Sullivan, C. W. (1985). Sea ice microbial communities. V. The vertical zonation of diatoms in an Antarctic fast ice community. *Journal of Phycology*, *21*(3), 401–409. https://doi.org/10.1111/j.0022-3646.1985.00401.x

Günther, S., & Dieckmann, G. S. (1999). Seasonal development of algal biomass in snow-covered fast ice and the underlying platelet layer in the Weddell Sea, Antarctica. *Antarctic Science*, *11*(3), 305–315. https://doi.org/10.1017/S0954102099000395

Hawes, I., Lund-Hansen, L. C., Sorrell, B. K., Nielsen, M. H., Borzák, R., & Buss, I. (2012). Photobiology of sea ice algae during initial spring growth in Kangerlussuaq, West Greenland: Insights from imaging variable chlorophyll fluorescence of ice cores. *Photosynthesis Research*, *112*(2), 103–115. https://doi.org/10.1007/s11120-012-9736-7

Kauko, H. M., Taskjelle, T., Assmy, P., Pavlov, A. K., Mundy, C. J., Duarte, P., et al. (2017). Windows in Arctic sea ice: Light transmission and ice algae in a refrozen lead. *Journal of Geophysical Research: Biogeosciences*, *122*, 1486–1505. https://doi.org/10.1002/2016JG003626

Kishino, M., Takahashi, M., Okami, N., & Ichimura, S. (1985). Estimation of the spectral absorption-coefficients of phytoplankton in the sea. *Bulletin of Marine Science*, *37*(2), 634–642.

Lange, B. A., Katlein, C., Nicolaus, M., Peeken, I., & Flores, H. (2016). Sea ice algae chlorophyll *a* concentrations derived from under-ice spectral radiation profiling platforms. *Journal of Geophysical Research: Oceans*, *121*, 8511–8534. https://doi.org/10.1002/2016JC011991

Langhorne, P. J., Hughes, K. G., Gough, A. J., Smith, I. J., Williams, M. J. M., Robinson, N. J., et al. (2015). Observed platelet ice distributions in Antarctic sea ice: An index for ocean-ice shelf heat flux. *Geophysical Research Letters*, *42*, 5442–5451. https://doi.org/10.1002/2015GL064508

Legendre, L., & Gosselin, M. (1991). In situ spectroradiometric estimation of microalgal biomass in first-year sea ice. *Polar Biology*, *11*(2), 113–115. https://doi.org/10.1007/BF00234273

Leu, E., Mundy, C., Assmy, P., Campbell, K., Gabrielsen, T., Gosselin, M., et al. (2015). Arctic spring awakening—Steering principles behind the phenology of vernal ice algal blooms. *Progress in Oceanography*, *139*, 151–170. https://doi.org/10.1016/j.pocean.2015.07.012

McMinn, A., Pankowskii, A., Ashworth, C., Bhagooli, R., Ralph, P., & Ryan, K. (2010). In situ net primary productivity and photosynthesis of Antarctic sea ice algal, phytoplankton and benthic algal communities. *Marine Biology*, *157*(6), 1345–1356. https://doi.org/10.1007/s00227-010-1414-8

Meiners, K. M., Arndt, S., Bestley, S., Krumpen, T., Ricker, R., Milnes, M., et al. (2017). Antarctic pack ice algal distribution: Floe-scale spatial variability and predictability from physical parameters. *Geophysical Research Letters*, *44*, 7382–7390. https://doi.org/10.1002/2017GL074346

Meiners, K. M., Vancoppenolle, M., Thanassekos, S., Dieckmann, G. S., Thomas, D. N., Tison, J.-L., et al. (2012). Chlorophyll *a* in antarctic sea ice from historical ice core data. *Geophysical Research Letters*, *39*, L21602. https://doi.org/10.1029/2012GL053478

Melbourne-Thomas, J., Meiners, K., Mundy, C., Schallenberg, C., Tattersall, K., & Dieckmann, G. (2015). Algorithms to estimate Antarctic sea ice algal biomass from under-ice irradiance spectra at regional scales. *Marine Ecology Progress Series*, *536*, 107–121. https://doi.org/10.3354/meps11396

Melbourne-Thomas, J., Meiners, K., Mundy, C., Schallenberg, C., Tattersall, K., & Dieckmann, G. (2016). Corrigendum: Algorithms to estimate Antarctic sea ice algal biomass from under-ice irradiance spectra at regional scales. *Marine Ecology Progress Series*, *561*, 261.

Mitchell, B. G. (1990). Algorithms for determining the absorption coefficient for aquatic particulates using the quantitative filter technique. *Proceedings of SPIE*, *1302*, 137–148. https://doi.org/10.1117/12.21440

Moreçki, V. N. (1965). Underwater sea ice. *Problemy Arktiki i Antarktiki*, *19*, 32–38 (translation by E. R. Hope, DRB Canada Rep. T497R, April 1968).

Morel, A., & Bricaud, A. (1981). Theoretical results concerning light absorption in a discrete medium, and application to specific absorption of phytoplankton. *Deep Sea Research Part A. Oceanographic Research Papers*, *28*(11), 1375–1393. https://doi.org/10.1016/0198-0149(81)90039-X

Müller, J. L., Bidigare, R., Trees, R. C., Balch, W. M., & Dore, J. (2003). *Ocean optics protocols for satellite ocean colour sensor validation, revision 5, volume V: Biogeochemical and bio-optical measurements and data* (NASA Tech. Memo.).

Mundy, C. J., Barber, D. G., & Michel, C. (2005). Variability of snow and ice thermal, physical and optical properties pertinent to sea ice algae biomass during spring. *Journal of Marine Systems*, *58*(3–4), 107–120. https://doi.org/10.1016/j.jmarsys.2005.07.003

Mundy, C. J., Ehn, J. K., Barber, D. G., & Michel, C. (2007). Influence of snow cover and algae on the spectral dependence of transmitted irradiance through Arctic landfast first-year sea ice. *Journal of Geophysical Research*, *112*, C03007. https://doi.org/10.1029/2006JC003683

Nicolaus, M., & Katlein, C. (2013). Mapping radiation transfer through sea ice using a remotely operated vehicle (ROV). *The Cryosphere*, *7*(3), 763–777. https://doi.org/10.5194/tc-7-763-2013

Nicolaus, M., Katlein, C., Maslanik, J., & Hendricks, S. (2012). Changes in Arctic sea ice result in increasing light transmittance and absorption. *Geophysical Research Letters*, *39*, L24501. https://doi.org/10.1029/2012GL053738

O'Reilly, J. E., Maritorena, S., Mitchell, B. G., Siegel, D. A., Carder, K. L., Garver, S. A., et al. (1998). Ocean color chlorophyll algorithms for SeaWiFS. *Journal of Geophysical Research*, *103*(C11), 24937–24953. https://doi.org/10.1029/98JC02160

Perovich, D. K. (2017). Sea ice and sunlight. In D. N. Thomas (Ed.), *Sea ice* (pp. 110–137). Hoboken, NJ: John Wiley. https://doi.org/10.1002/9781118778371.ch4

Perovich, D. K., Cota, G. F., Maykut, G. A., & Grenfell, T. C. (1993). Bio-optical observations of first-year Arctic sea ice. *Geophysical Research Letters*, *20*(11), 1059–1062. https://doi.org/10.1029/93GL01316

Smith, I. J., Gough, A. J., Langhorne, P. J., Mahoney, A. R., Leonard, G. H., Hale, R. V., et al. (2015). First-year land-fast Antarctic sea ice as an archive of ice shelf meltwater fluxes. *Cold Regions Science and Technology*, *113*, 63–70. https://doi.org/10.1016/j.coldregions.2015.01.007

Smith, I. J., Langhorne, P. J., Haskell, T. G., Trodahl, H. J., Frew, R., & Vennell, M. R. (2001). Platelet ice and the land-fast sea ice of McMurdo Sound, Antarctica. *Annals of Glaciology*, *33*(1), 21–27. https://doi.org/10.3189/172756401781818365

Sturm, M., & Massom, R. A. (2017). Snow in the sea ice system: Friend or foe? In D. N. Thomas (Ed.), *Sea ice* (pp. 65–109). Hoboken, NJ: John Wiley. https://doi.org/10.1002/9781118778371.ch3

Tamura, T., Ohshima, K. I., Fraser, A. D., & Williams, G. D. (2016). Sea ice production variability in Antarctic coastal polynyas. *Journal of Geophysical Research: Oceans*, *121*, 2967–2979. https://doi.org/10.1002/2015JC011537

van Leeuwe, M. A., Tedesco, L., Arrigo, K. R., Assmy, P., Campbell, K., Meiners, K. M., et al. (2018). Microalgal community structure and primary production in Arctic and Antarctic sea ice: A synthesis. *Elementa: Science of the Anthropocene*, *6*, 4. https://doi.org/10.1525/elementa.267

Weeks, W. (2010). *On sea ice*. Fairbanks: University of Alaska Press.